Amino Acids (2022) 54:1261–1274
https://doi.org/10.1007/s00726-022-03178-w

ORIGINAL ARTICLE

Photochemical synthesis of pink silver and its use for monitoring peptide nitration via surface enhanced Raman spectroscopy (SERS)

Marina Sokolová[1] · Hana Šestáková[1] · Martin Truksa[2] · Martin Šafařík[1] · Romana Hadravová[1] · Petr Bouř[1] · Jaroslav Šebestík[1,2]

Received: 13 January 2022 / Accepted: 31 May 2022 / Published online: 22 June 2022

Abstract

Oxidative stress may cause extended tyrosine posttranslational modifications of peptides and proteins. The 3-nitro-L-tyrosine (Nit), which is typically formed, affects protein behavior during neurodegenerative processes, such as Alzheimer's and Parkinson's diseases. Such metabolic products may be conveniently detected at very low concentrations by surface enhanced Raman spectroscopy (SERS). Previously, we have explored the SERS detection of the Nit NO_2 bending vibrational bands in a presence of hydrogen chloride (Niederhafner et al., Amino Acids 53:517–532, 2021, ibid). In this article, we describe performance of a new SERS substrate, "pink silver", synthesized photochemically. It provides SERS even without the HCl induction, and the acid further decreases the detection limit about 9 times. Strong SERS bands were observed in the asymmetric (1550–1475 cm^{-1}) and symmetric (1360–1290 cm^{-1}) NO stretching in the NO_2 group. The bending vibration was relatively weak, but appeared stronger when HCl was added. The band assignments were supported by density functional theory modeling.

Keywords Nitration · Oxidative stress · Surface enhanced Raman spectroscopy (SERS) · Photochemical synthesis · Silver colloids · Posttranslational protein modification (PTM)

Abbreviations

ACN	Acetonitrile
Bn	Benzyl
CCT	Cartesian coordinate-based tensor transfer method
DIC	*N,N′*-Diisopropylcarbodiimide
DMF	*N,N*-Dimethylformamide
EDT	1,2-Ethanedithiol
ESI	Electrospray ionization
Fmoc	9-Fluorenylmethoxycarbonyl
GSH	Glutathione
HOBt	*N*-Hydroxybenzotriazole
HPLC	High-performance liquid chromatography
MD	Molecular dynamics
MS	Mass spectrometry
Nit	3-Nitro-L-tyrosine
PTM	Posttranslational modification
ROA	Raman optical activity
SERS	Surface-enhanced Raman spectroscopy
tBu	Tert-Butyl
TEM	Transmission electron microscopy
TFA	Trifluoroacetic acid
TIS	Triisopropyl silane

Introduction

Reactive oxygen and nitrogen species fulfill many important physiological and pathological functions (Madkour 2019; Beckman et al. 1990; Beckman and Crow 1993; Ježek et al. 2017). They serve as signaling molecules, and are generated by the immune system as a defense against pathogens (Radi 2004, 2013). However, if present in high concentrations they cannot be handled by the protective mechanisms based on antioxidants, and oxidative stress occurs (Sies 2020; Forman and Zhang 2021). This state is implicated, for example, in diabetes mellitus type 2, or in

✉ Jaroslav Šebestík
sebestik@uochb.cas.cz

[1] Institute of Organic Chemistry and Biochemistry, Academy of Sciences, Flemingovo náměstí 2, 16610 Prague 6, Czech Republic

[2] Mensa Gymnázium O.P.S., Španielova 1111/19, 163 00 Prague 6, Czech Republic

many neurodegenerative diseases (Ježek et al. 2017; Sies 2020; Forman and Zhang 2021).

Nitration-accompanied changes of proteins are important post-translational modifications (PTM) (Larsen et al. 2006; Tsikas and Duncan 2014) as they affect protein functioning. For instance, nitration of tyrosine or crosslinking of two tyrosines leads to protein oligomerization (Radi 2004, 2013; Reynolds et al. 2005; Vana et al. 2011). We focus on 3-nitro-L-tyrosine (Nit), which is probably the most frequent PTM in proteins (Abello et al. 2009; Castro et al. 2011; Aslan and Dogan 2011; Yttenberg and Jensen 2010; Campolo et al. 2020).

The nitration is an early-stage marker of oxidative stress and neurodegeneration. The presence of Nit was observed in the post-mortem brains and cerebrospinal fluids of patients with Alzheimer's disease (AD), Parkinson's disease (PD), and amyotrophic lateral sclerosis (Reynolds et al. 2005; Burai et al. 2015; Meade et al. 2019; Ouesla ti et al. 2010; Beal et al. 1997). An increasing level of nitrotyrosine seems to correspond to progression of the Parkinson's disease and its severity (Gupta et al. 2021).

The nitration of tyrosine significantly decreases the pK_a value of the hydroxyl group, affects hydrophobicity of the residue, often alters protein structure, and in many cases leads to the loss of biological functions of the proteins (Ferrer-Sueta et al. 2018; Sevcsik et al. 2011; Kummer et al. 2011; Campolo et al. 2020). It enhances aggregation of α-synuclein (Giasson et al. 2000) or amyloid β (Kummer et al. 2011), and promotes formation of specific protein inclusions (Duda et al. 2000; Giasson et al. 2000).

A tool for reliable detection and quantification of oxidized forms of amino acids in proteins can thus be useful for diagnosis of various diseases and disorders related to the oxidative stress. Classical methods for detection of Nit in proteinogenic samples are based on HPLC chromatography, UV–Vis spectroscopy, and amino acid analysis (Furth and Hope 1970; Beeckmans and Kanarek 1983). The detection is a challenge since its concentration is relatively very low (Zhao et al. 2017). A more versatile method is tandem mass spectrometry in combination with either gas chromatography (GC–MS, GC–MS/MS) or liquid chromatography (LC–MS/MS) (Larsen et al. 2006; Tsikas and Duncan 2014; Seeley et al. 2014). These methods can sense Nit to sub nM or sometimes pM levels. Also gold nanoparticles (AuNP) captured in metal–organic framework served as a good sensor of free Nit, with 1.8 nM limit of detection (LOD) (Jalili et al. 2020; Martins et al. 2018, 2020; Zhai et al. 2019). The detection can be combined with a Nit selective enrichment (Abello et al. 2010; Zhao et al. 2017), or its conversion to other residues (Liu et al. 2019; Abello et al. 2010; Sangsuwan et al. 2016; van Haandel et al. 2008; Sharov et al. 2010; Soderling et al. 2007; De Filippis et al. 2006).

Detection by surface-enhanced Raman spectroscopy (SERS) works for sub mM levels (Seballos et al. 2007; Kurouski et al. 2017) and can be done with various substrates (Kurouski et al. 2017; Guerrini and Graham 2012; Zhang et al. 2014a, b; Betz et al. 2014; Kleinman et al. 2013; Sharma et al. 2012; Mulvihill et al. 2010; Rycenga et al. 2012; Shao et al. 2013; Jing et al. 2014; Zhang et al. 2014a, b; Graham et al. 2008; Taylor et al. 2011; Alvarez-Puebla et al. 2009). When colloids are used, they are often stabilized, for example, by citrate or cetyltrimethylammonium bromide. This, however, may provide unwanted SERS signals (Kurouski and van Duyne 2015; Martinsson et al. 2015). Leopold and Lendl (2003) prepared "surfactant free" nanoparticles.

Some strategies also use the photosensitivity of silver and its compounds. Nanoprisms were produced with a green light (with wavelength of ~ 550 nm) (Xue et al. 2008). Nanodecahedra were prepared from silver nitrate/citrate solution by irradiation with the blue light (~ 460 nm) (Yang et al. 2012). Various shapes of nanoparticles were obtained using intensive sunlight in Mexico (Félix-Domínguez et al. 2019). The nanoparticle shape was also influenced by the light intensity (Huang et al. 2019).

Previously, we used SERS for monitoring the tyrosine nitration based on AgNP aggregation with hydrogen chloride (Niederhafner et al. 2021). The nitration could be detected, but problems with colloid stability appeared. In the present article, we designed a photoreactor where silver nanoparticles are produced upon sample illumination. We also describe two protocols for detection of nitrotyrosine in a model peptide, YYACAYY (Fig. 1), used in material science (Lee et al. 2016, 2019). The peptide contains four tyrosine residues available for nitration and cysteine needed for anchoring the peptide on the silver surface. Thus, we have synthesized one native YYACAYY and 15 Nit modified peptides.

Experimental part

General procedures and chemicals

Three batches of $AgNO_3$ purchased from Sigma-Aldrich were used, cat. no. 209139 (> 99.0%, batches MKBD2163V (99.2%) and MKCP2378 (99.6%)), and cat. no. 204390 (99.9999%, batch 0000075290). Trisodium citrate dihydrate was obtained from Sigma-Aldrich as well (cat. no. S1804, batch 020M0026V).

Peptide synthesis

Peptides were synthesized with the Fmoc/tBu method (Fields and Noble 1990) by manual solid-phase synthesis

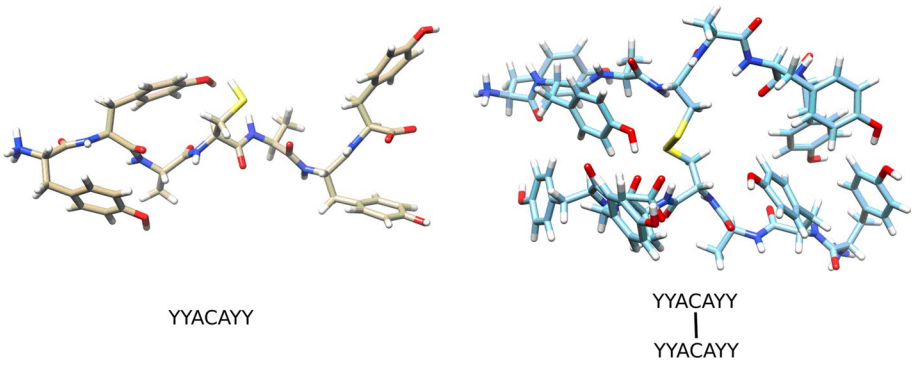

Fig. 1 Examples of simulated (MD) structures of the model peptide YYACAYY in monomeric and dimeric forms

using quadruple molar excess of Fmoc-protected amino acids (0.21 mmol) and coupling reagents DIC (33 µL; 0.21 mmol) and HOBt (28 mg; 0.21 mmol) in DMF (2 mL). To avoid contamination with 3,3'-dityrosine, nitrotyrosine containing peptides of required sequence were prepared from Fmoc-Nit(Bn)-OH (Niederhafner et al. 2016, 2021; Niederhafner et al. 2016). The peptides were cleaved from the resin by a mixture of TFA (4.5 mL), H_2O (150 µL), EDT (150 µL), thioanisole (150 µL), and TIS (50 µL) for 4 h, unless stated otherwise. Peptide deprotection was done during the cleavage from the resin. The Cys(tBu) group was kept to prevent peptide dimerization during its characterization, and it was cleaved spontaneously upon contact with the silver surface. All peptides were prepared in more than 95% purity (HPLC chromatograms and MS data are available in Supplementary Information).

Chromatographic and MS methods

During the syntheses, molecular weights of peptide fragments were determined using an electrospray ionization mass spectroscopy (ESI–MS). For HPLC, an instrument with a quaternary pump, thermostat, diode array detector and reverse-phase C_{18} columns were used. The peptides were purified by semipreparative HPLC on the VYDAC 250 × 10 mm, 10 µm RP-18 column with a flow rate 3 mL/min using a 0–100% ACN (acetonitrile) gradient in 0.05% aqueous TFA. Analytical HPLC was carried out with a Poroshell 120 SB-C18 2.7 µm, 3.0 × 50 mm column, flow rate 1 mL/min, and diode array detection using gradient 5–5-100–100% of ACN in 0.05% aqueous TFA within 0–1-11–13 min.

YYACAYY—H-Tyr-Tyr-Ala-Cys(tBu)-Ala-Tyr-Tyr-OH–HPLC: R_T 4.74 min. For $C_{49}H_{61}N_7O_{12}S$ (971.41) found ESI–MS, m/z: 972.42 ($M+H^+$), 994.40 ($M+Na^+$).

YYACAYNit—H-Tyr-Tyr-Ala-Cys(tBu)-Ala-Tyr-Nit-OH–HPLC: R_T 5.22 min. For $C_{49}H_{60}N_8O_{14}S$ (1016.39) found ESI–MS, m/z: 1017.40 ($M+H^+$), 1 039.38 ($M+Na^+$).

YYACANitY—H-Tyr-Tyr-Ala-Cys(tBu)-Ala-Nit-Tyr-OH–HPLC: R_T 4.96 min. For $C_{49}H_{60}N_8O_{14}S$ (1016.39) found ESI–MS, m/z: 960.27 (M-tBu^+).

YNitACAYY—H-Tyr-Nit-Ala-Cys(O)(tBu)-Ala-Tyr-Tyr-OH–HPLC: R_T 5.08 min. For $C_{49}H_{60}N_8O_{15}S$ (1032.39) found ESI–MS, m/z: 1033.40 ($M+H^+$).

NitYACAYY—H-Nit-Tyr-Ala-Cys(tBu)-Ala-Tyr-Tyr-OH–HPLC: R_T 4.96 min. For $C_{49}H_{60}N_8O_{14}S$ (1016.39) found ESI–MS, m/z: 1017.40 ($M+H^+$), 1039.38 ($M+Na^+$).

YYACANitNit—H-Tyr-Tyr-Ala-Cys(tBu)-Ala-Nit-Nit-OH–HPLC: R_T 5.56 min. For $C_{49}H_{59}N_9O_{16}S$ (1061.38) found ESI–MS, m/z: 1062.39 ($M+H^+$).

YNitACAYNit—H-Tyr-Nit-Ala-Cys(tBu)-Ala-Tyr-Nit-OH–HPLC: R_T 5.52 min. For $C_{49}H_{59}N_9O_{16}S$ (1061.38) found ESI–MS, m/z: 1062.39 ($M+H^+$).

NitYACAYNit—H-Nit-Tyr-Ala-Cys(tBu)-Ala-Tyr-Nit-OH–HPLC: R_T 5.40 min. For $C_{49}H_{59}N_9O_{16}S$ (1061.38) found ESI–MS, m/z: 1062.39 ($M+H^+$).

YNitACANitY—H-Tyr-Nit-Ala-Cys(tBu)-Ala-Nit-Tyr-OH–HPLC: R_T 5.43 min. For $C_{49}H_{59}N_9O_{16}S$ (1061.38) found ESI–MS, m/z: 1062.39 ($M+H^+$).

NitYACANitY—H-Nit-Tyr-Ala-Cys(tBu)-Ala-Nit-Tyr-OH–HPLC: R_T 5.29 min. For $C_{49}H_{59}N_9O_{16}S$ (1061.38) found ESI–MS, m/z: 1062.39 ($M+H^+$).

NitNitACAYY—H-Nit-Nit-Ala-Cys(O)(tBu)-Ala-Tyr-Tyr-OH–HPLC: R_T 5.30 min. For $C_{49}H_{59}N_9O_{17}S$ (1077.37) found ESI–MS, m/z: 1078.05 ($M+H^+$).

YNitACANitNit—H-Tyr-Nit-Ala-Cys(tBu)-Ala-Nit-Nit-OH–HPLC: R_T 5.89 min. For $C_{49}H_{58}N_{10}O_{18}S$ (1106.37) found ESI–MS, m/z: 1107.37 ($M+H^+$).

NitYACANitNit—H-Nit-Tyr-Ala-Cys(tBu)-Ala-Nit-Nit-OH–HPLC: R_T 5.80 min. For $C_{49}H_{58}N_{10}O_{18}S$ (1106.37) found ESI–MS, m/z: 1107.37 ($M+H^+$).

NitNitACAYNit—H-Nit-Nit-Ala-Cys(tBu)-Ala-Tyr-Nit-OH–HPLC: R_T 5.73 min. For $C_{49}H_{58}N_{10}O_{18}S$ (1106.37) found ESI–MS, m/z: 1107.37 ($M+H^+$).

NitNitACANitY—H-Nit-Nit-Ala-Cys(O)(tBu)-Ala-Nit-Tyr-OH–HPLC: R_T 5.29 min. For $C_{49}H_{58}N_{10}O_{19}S$ (1122.36) found ESI–MS, m/z: 1162.23 ($M+K+H^+$).

NitNitACANitNit—H-Nit-Nit-Ala-Cys(tBu)-Ala-Nit-Nit-OH–HPLC: R_T 6.07 min. For $C_{49}H_{57}N_{11}O_{20}S$ (1151.35) found ESI–MS, m/z: 1152.36 ($M+H^+$).

Crystallization of $AgNO_3$

A procedure of Özmetin et al. 2001 was adopted. One gram of $AgNO_3$ was dissolved in warm HNO_3 (65%, 20 mL, 70 °C). The solution was left to cool down, and crystals were filtered off and dried in desiccator over Na_2CO_3 in darkness. Yield 0.7 g.

Photoreactor

A photoreactor was constructed using Arduino Nano and phototransistor TEMT6000 for monitoring the progress of synthesis (Fig. 2). Source of power was 2 × USB-A, 5 V/2.4A charger (GB 44,952; GME 781–005). For driving of LED fields, NPN transistors (2N2219A, 40 V, 0.8A, 3 W; GME 215–317) were used in the scheme labeled by QXpow. LED diodes were used for illumination at 395 nm (5 mm Round UV LED, OSV4DL5111A; GME 518–400; 1 mW at the sample), 470 nm (Deluxe Power 5 mm Round Blue; OSB56L5111P; GME 518–104; 20 mW at the sample), 525 nm (5 mm Round Ultra Bright Pure Green LED OSG5GP5111A; GME 518–451; 10 mW at the sample), and 568 nm (5 mm, Green LED BL-B2434; GME 511–226; 20 µW at the sample), respectively. The intensity of light at the sample was measured using a laser power meter (Thorlabs PM100USB) with photodiode power sensor (Si, 400–1100 nm, 500 mW, no. S121C). We used a TEMT6000 phototransistor to measure the light intensity at 395 nm passed through the sample (0°, absorption), at 470 nm for 90° scattering, at 525 nm (90° scattering), and 568 nm (180°, back-scattering). The signal was recorded at 0 min, 4 min, 14 min, and then every 10 min for all four wavelengths.

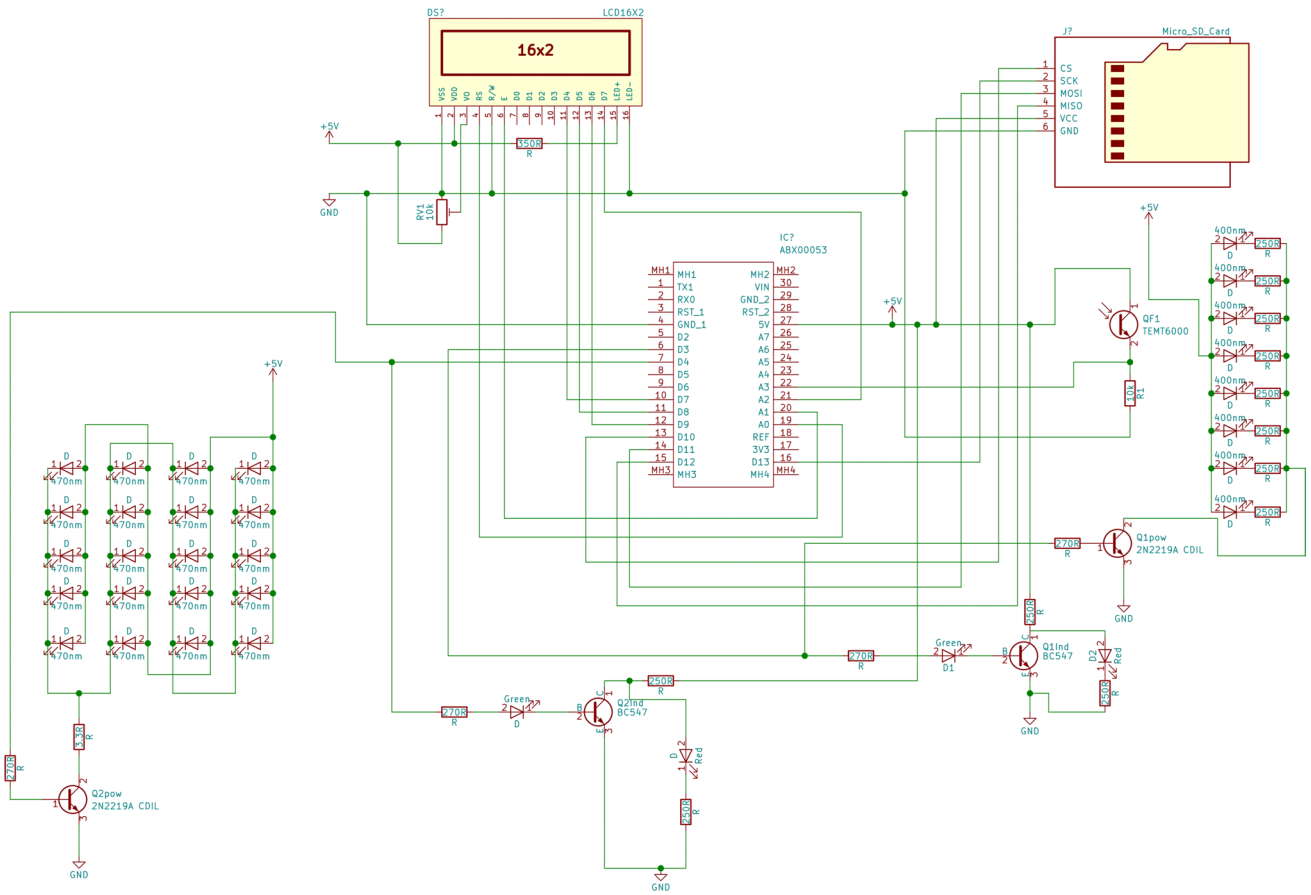

Fig. 2 Electronics of the photoreactor. For clarity, connections of D5 and D6 to other LED diode field are not depicted (they resemble the connections to the LED field and indicating diodes driven by transistors Q2pow and Q2Ind). The field of green diodes (525 nm) connected to D5 has the same number of diodes as the blue field (470 nm) connected to D4. The other green field (568 nm) connected to D6 contains 17 LED diodes instead of 20 due to placement of phototransistor TEMT6000 for monitoring. UV-LEDs (395 nm) are connected to pin D3 and this field contains only 8 diodes. IC ABX00053 stands for Arduino Nano

Photochemical synthesis of pink silver

Amber glass bottle was cleaned by KOH/EtOH solution (Mulfinger et al. 2007) before preparation of a stock solution of 0.2 mM $AgNO_3$ (34 mg/L) and 1 mM trisodium citrate dihydrate (294 mg/L). The solution was irradiated in the photoreactor at 470 nm for 17.5 h unless stated otherwise. TEMT6000 data were logged at 0 min, 4 min, 14 min, and every other 10 min for all four wavelengths. To obtain the pink silver, the stock solution needed to be stored in dark for at least 7 days and less than 110 days.

UV–Vis spectra

UV–Vis spectra for stock solutions, nanoparticles, and their mixtures were measured using a WTW PhotoLab7600 spectrometer. The samples were held in 1 cm path plastic cells, spectral range was from 250 to 1100 nm, step 1 nm.

Raman and SERS spectra

Raman spectra acquired with a BioTools ChiralRAMAN-2X instrument (532 nm excitation wavelength; spectral range 90–2320 cm^{-1}) were processed using a homemade software (Šebestík and Bouř 2011; Šebestík et al. 2012). SERS has been used to detect GSH and peptide nitration in a series of 16 model peptides after loading the peptides on silver nanoparticles. For "induced SERS" measurement (Niederhafner et al. 2021; Das et al. 2021), 1 M HCl was added for suppression of colloidal background and the spectra were obtained for mixtures of Ag sol (90 µL), 10^{-3} M sample solution (10 µL), and 1 M HCl (10 µL) with 3.30 s illumination time per scan. For "native SERS", HCl was not added. For control, Raman and SERS spectra were also acquired with Ocean Optics QEPro instrument (785 nm excitation wavelength, 300 mW at the sample; spectral range 200–4066 cm^{-1}).

Transmission electron microscopy (TEM)

Parlodion-carbon-coated copper grids were first transferred to a droplet of poly(ethyleneimine) (2.5 kDa, 0.1 mg/mL) and incubated for 10 min. Then the grids were washed in water for 10 min. Finally, the grids were transferred on the top of drop of aqueous solution of silver sol and removed after 5 min. TEM images were captured using a JEOL JEM-1011 electron microscope operated at 80 kV.

Calculations

Starting geometries of the peptides were obtained by molecular dynamics (MD) simulations performed using the Amber12 program (Case et al. 2012). Unconstrained dynamics of wild-type YYACAYY and dimeric YYACAYY were run for 40 ns, with the Amber12SB force field in a box of water $40\times40\times40$ $Å^3$. From the MD trajectory, a set of snapshots was selected using a density-based clustering algorithm implemented in cpptraj (AmberTools) with three minimum points for a cluster, the distance cutoff for forming a cluster (ε) was set to 1.1 Å for YYACAYY and 1.2 Å for dimeric structure, the sieve to frame options was on, and coordinate root-mean-squared deviation distance metric was used with sieve 10. For optimization of ε size, see our previous work (Niederhafner et al. 2021). The most abundant structures of YYACAYY and its dimeric form are shown in Fig. 1.

A model brick of 640 Ag atoms and volume $30\times19\times15$ $Å^3$ was constructed, and the most abundant conformer of YYACAYY was anchored by the S_{Cys}-Ag bond to either a corner, edge, or plane (Fig. 3). Lennard–Jones potentials for Ag were used (Heinz et al. 2008, 2009). Free

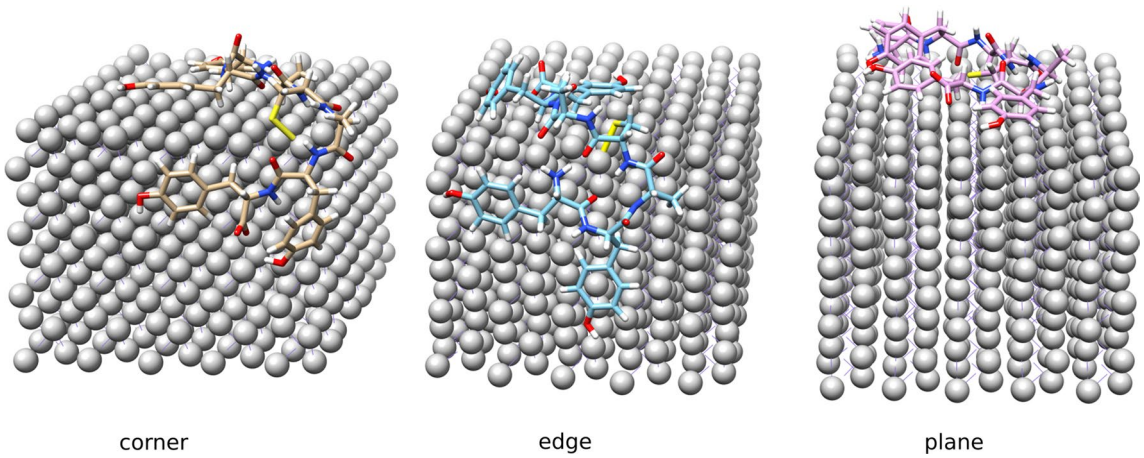

Fig. 3 Peptide YYACAYY anchored to the corner, edge, and plane of the silver box

dynamics was run for 100 ns, with the Amber12SB force field for the peptide. For silver atoms, a restrain force constant 20 kcal × mol^{-1} × Å^{-2} was applied to maintain the crystal structure. A set of snapshots was selected using the density-based clustering algorithm [3 minimum points for a cluster, distance cutoff (ε) 0.5 Å, sieve to frame options on, and coordinate root-mean-squared deviation distance metric with sieve 2].

The peptides bound on the silver obtained from MD were used as starting structures in quantum-chemical calculations, using the Gaussian16 program (Frisch et al. 2016). The number of silver atoms was limited by a php script to those closer than 3.5 Å to the peptide (Figure S1), and only close shells (even numbers of unbound silver atoms) were considered. The geometries were partially optimized at the HF/LanL2MB level with implicit CPCM/water solvent model (Tomasi et al. 2005; Klamt and Schürmann 1993) in vibrational normal mode coordinates, so that modes with frequency smaller than 300 cm^{-1} were fixed (Bouř and Keiderling 2002). The Ag-peptide complexes were split to smaller fragments (Figure S1) with the same php script, which introduces *N*- and *C*- capping of peptidic fragments with Ac and NHMe groups, β-carbon capping with hydrogens for aromatic fragments and for backbone fragments. The fragments were also optimized in the normal mode coordinates using the same frequency limit, but at a higher level, B3PW91/LanL2DZ (Perdew et al. 1996; Sue Legge et al. 2001), with the CPCM solvent model. For the optimized fragments, vibrational tensors at the B3PW91/LanL2DZ level needed for Raman/ROA intensities were calculated (Ruud and Thorvaldsen 2009, with 532 nm excitation) and transferred back onto the full peptide, using the Cartesian coordinate tensor transfer (CCT) method (Bouř et al. 1997; Yamamoto and Bouř 2013). Then within the harmonic approximation spectral intensities were calculated and the spectra plotted using Lorentzian bands and 10 cm^{-1} full width at half height.

Results and discussion

Peptide synthesis

The peptide was synthesized with tBu attached to the SH group (Spears et al. 2021). This protection prevented dimerization of the peptide via disulfide bridge formation, thus allowing easier peptide characterization. When exposed to silver surface, tBu spontaneously dissociated. This was confirmed by observation of SERS signal typical for Cys bound to the silver surface with bands at 625 cm^{-1} and 664 cm^{-1} (YYACAYY, Fig. 4), 662 cm^{-1} (GSH, Fig. 7b), and 620 and 674 cm^{-1} (Cys, reported for ν(C-S) depending on pH, Chang et al. 2019). The Ag–S stretching signal (231–236 cm^{-1},

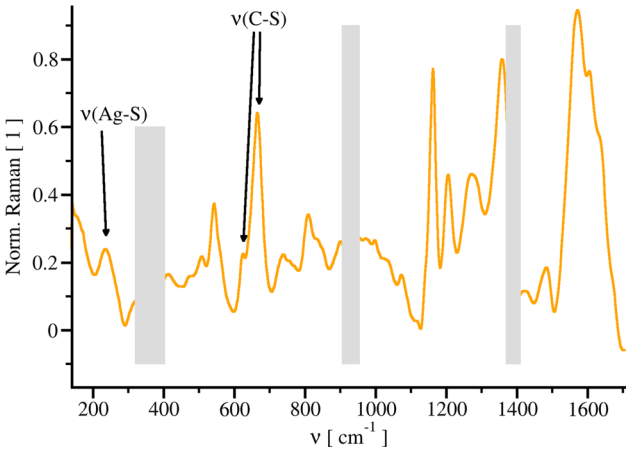

Fig. 4 SERS spectrum of YYACAYY peptide with subtracted ACN/colloid mixture. Vibrations confirming cleavage of tBu are indicated. Zones affected by the solvent are hidden by the gray bars (ACN bands at 383, 924 and 1376 cm^{-1})

Huang et al. 2010) was not observed on pink silver with GSH in water, because of a strong scattering of the colloid in this region (not shown). However, the ν(Ag–S) band was observed at 235 cm^{-1} after attaching YYACAYY to the silver surface in a ACN/water mixture (Fig. 4).

Photochemical synthesis of pink silver

At the beginning of photochemical synthesis, the light at 395 nm is strongly absorbed by the solution. After ca 150 min, the maximal absorption (minimal voltage) was achieved and then the absorption of that light started to slightly decrease (Fig. 5a). The pink silver obtained from batches younger than 8 days is meta-stable, and partially precipitated. The pink silver from older batches is more stable. However, with a stock solution over three years old a brown silver was obtained instead of the pink one (Figure S2a). The brown silver is very stable and can survive for several weeks without precipitation, but does not provide good SERS. An opposite extreme represent solutions younger than 5 days, giving a white silver (Figure S2j). This is very unstable and precipitates completely within a week. As the stock solution is aging, plasmonic absorption bands are increasing, and the ratio between higher- and lower-wavelength bands is decreasing.

Influence of silver nitrate on pink silver synthesis

The UV–Vis spectra of silver nitrate/citrate stock solutions indicate a presence of silver seeds formed by aging (Figure S3). When the silver nitrate stock solution was made from commercially available silver nitrate, absorbance at 400 nm (an indicator of nanosilver presence) was higher.

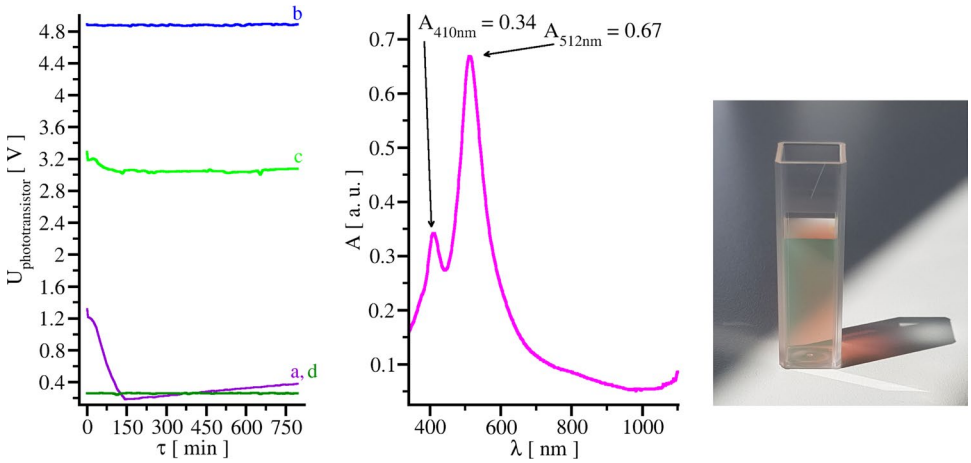

Fig. 5 (Left) progress of the pink silver synthesis monitored by TEMT6000 **a** 395 nm (0°, absorption); **b** 470 nm (90°, scattering); **c** 525 nm (90°, scattering); **d** 568 nm (180°, back-scattering).; (middle) UV–Vis spectrum of pink silver obtained from 7 days old stock solution after the synthesis; and (right) pink silver photography with green color visible in the front of the cell, with the colloid in shade. This is caused by a strong scattering of the green light

Crystallization of silver nitrate from concentrated nitric acid provided a solution with significantly lower absorbance at 400 nm. According to our experience, the presence of silver seeds indicated by the absorbance at 400 nm was necessary for preparation of the pink silver. Otherwise a meta-stable white silver was formed.

Influence of the light wavelength on pink silver synthesis

We tried four different wavelengths. From Figure S4 and Table 1, we see that the ratio of the two plasmonic bands depends on them. To achieve higher absorbance of the second plasmonic band, a co-irradiation with violet light (395 nm) is desirable (Figure S4 cf. a–c). Co-irradiation with the green light (525 nm) led to a red-shift of the second plasmonic band (cf. c and f–h). Prolongation of radiation with the blue light alone also resulted in an increase of the second and a decrease of the first band (cf. c and d). Even longer radiation caused deformation of the second plasmonic band (probably composite of more plasmonic bands, cf. c and e). Interestingly, when the stock solution of silver nitrate and citrate was exposed to a weak ambient light for 12 days, nanosilver with two plasmonic bands was

Table 1 Positions and intensities of absorbance maxima of photochemically synthesized (pink) silver

Label[a]	Illumination time [h]	Illumination wavelength 470 nm + co-illumination light wavelength + time of co-illumination/ illumination driving period	λ_1 [nm]	$A_{\lambda 1}$ [a. u.]	λ_2 [nm]	$A_{\lambda 2}$ [a. u.]
a	24	395 nm 4.90 min/5 min	401	0.98	514	1.18
b	24	395 nm 1 min/5 min	410	0.87	517	1.00
c	24	–	411	0.92	515	0.84
d	48	–	418	0.74	512	0.92
e	72	–	418	0.69	509[c]	0.90
f	24	525 nm 10 s/5 min	415	0.89	519	0.85
g	24	525 nm 1 min/5 min	414	0.86	523	0.91
h	24	525 nm 2 min/5 min	415	0.85	529	0.85
i	0	–[b]	422	0.13	575	0.07

[a]cf. Figure S4

[b]Ambient light in a shadow place for 12 days

[c]The peak seems to be composed from more subbands

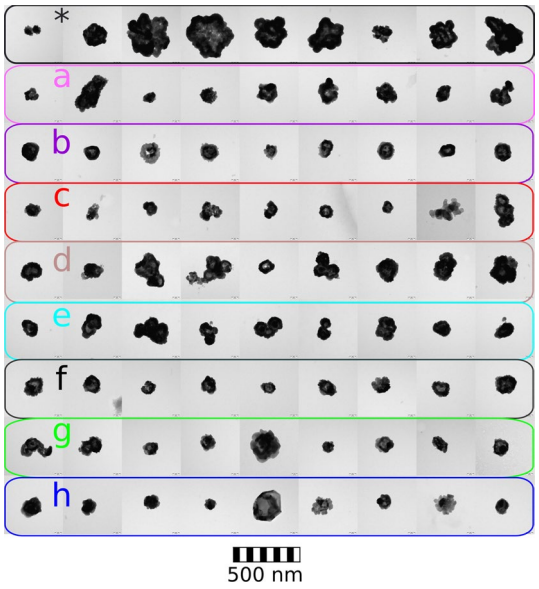

Fig. 6 TEM images of silver nanoparticles prepared using under various light illuminations. For their UV–Vis spectra see Figure S4 and Table 1. All samples were illuminated continuously at 470 nm, 20 mW on the sample. **a** co-illumination with 395 nm (1 mW) for 4.90 min/5 min; 105 days old stock; **b** co-illumination with 395 nm (1 mW) for 1 min/5 min; 101 days old stock; **c** no–co-illumination; 92 days old stock; **d** no–co-illumination, 48 h; 99 days old stock; **e** no–co-illumination, 72 h; 102 days old stock; **f** co-illumination with 525 nm (10 mW) for 10 s/5 min; 91 days old stock; **g** co-illumination with 525 nm (10 mW) 1 min/5 min; 93 days old stock; **h** co-illumination with 525 nm (10 mW) 2 min/5 min; 94 days old stock. Sample labeled with asterisk was irradiated at 470 nm for 17.5 h with regular checking of absorbance, and scattering at 395, 470, 525, and 568 nm from 7 days old stock (for UV–Vis see Fig. 5)

also formed (Figure S4, i), with absorbance at 10% of that for the sample from the photoreactor after 24 h irradiation.

Stability of the pink silver in the presence of YYACAYY peptide

When the pink silver was exposed to YYACAYY peptide (114 μM), it was stable for 12 min without significant change of UV–Vis spectra (Figure S5, a–c). The situation became different in the presence of HCl, when the pink silver was unstable (c.f. a,d–e). The presence of YYACAYY peptide (104 μM) led to partial stabilization of the pink silver (c.f. d and f; and e and g). We suppose that the stabilization is caused by covalent binding of the peptide to the silver surface. During peptide controlled aggregation of the pink silver, another plasmonic band around 700 nm appeared (Figure S5, g).

TEM

In previously published photochemical syntheses of nanosilver (Xue et al. 2008; Yang et al. 2012), the authors obtained well-defined nanoprisms (Xue et al. 2008), or nanodecahedra (Yang et al. 2012). In our photoreactor using lower concentration of sodium citrate, the dispersion of nanoparticle sizes was much higher and shapes were not regular (Fig. 6). Only with a co-illumination with 525 nm more regular nanoparticles were obtained (Fig. 6h).

SERS

Below, we distinguish native SERS, achieved with mixing of pink silver with analyte, and induced SERS, where also

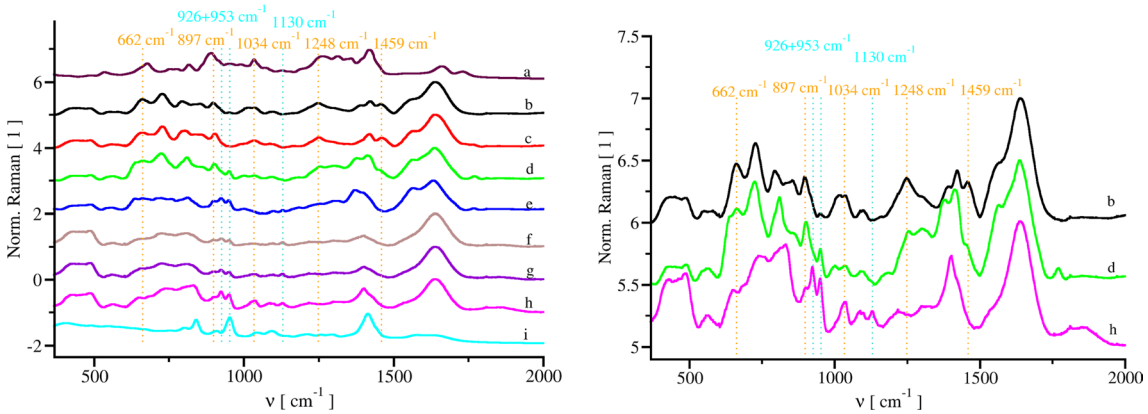

Fig. 7 Detection of GSH using pink silver and green laser 532 nm. **a** Raman spectrum of GSH (0.28 M, 900 mW, 2.5 s illumination time); **b** GSH + pink silver (175 μM, 300 mW, 3.01 s illumination time) **c** GSH + pink silver (8.8 μM); **d** GSH + pink silver (880 nM); **e** GSH + pink silver (440 nM); **f** GSH + pink silver (176 nM); **g** GSH + pink silver (88 nM); **h** pink silver + water (300 mW, 3.01 s illumination time); **i** Raman spectrum of sodium citrate (0.52 M, 500 mW, 3.01 s illumination). Orange dotted lines represent signals related to presence of GSH, cyan dotted lines show dominance of citrate (stabilizer of the silver nanoparticles). On the right panel SERS spectra of silver nanoparticles with water (h) and with GSH (b, d) are enlarged

HCl is present, HCl acts as an activator/initiator of the silver precipitation and a suppressor of citrate SERS spectrum (Niederhafner et al. 2021). pH of the samples during these two modes is different and so are SERS spectra.

First, the SERS performance of the pink silver was investigated on GSH (Fig. 7), which binds to the silver surface via the sulfhydryl group of cysteine. Comparison of normal Raman spectra with SERS for GSH (cf. a and b) and citrate (cf. i and h) revealed that SERS frequencies can be both red or blue shifted. GSH could be detected on pink silver down to 880 nM concentration (Fig. 7d) by bands at 662, 897, 1248, and 1459 cm^{-1}, using the 532 nm excitation. Bands at 662, 1248, and 1459 cm^{-1} are solely presented in spectra containing GSH (i.e. b and d, but not h in zoomed panel). In presence of GSH, the 897 cm^{-1} band is much stronger than those at 926 and 953 cm^{-1}. The 1034 cm^{-1} band is present both with and without GSH; in the former case it can be accompanied by another peak. At 880 nM GSH concentration, the citrate band at 953 cm^{-1} is apparent. At 440 nM GSH concentration, another citrate band at 1130 cm^{-1} appeared (Fig. 7e).

The influence of the silver substrate on SERS of GSH was also examined (Figure S6). Short pulses of co-illumination with violet or green light led to silver substrates providing weak SERS (Figure S6b+,f+). Longer co-illumination with violet light enhanced signals at 1423 cm^{-1} (cf a+ and c+). Similar enhancement was observed in pink silver solution from a fresh stock (Figure S6*+). Longer co-illumination with green light led to enhancement of the 1471 cm^{-1} band (g+ and h+), co-illumination with violet light led to suppression of the band at 1557 cm^{-1} (cf a+, c+, h+). Interestingly, the signal below 1000 cm^{-1} was conserved for most silver substrates, with exceptions of b+ and f+. Thus the light used for the photochemical production of the silver substrate can significantly influence the substrate capability of SERS.

Since the second plasmonic band of the pink silver shifts to the red, the SERS was also investigated using the 785 nm laser excitation (Fig. 8). The Raman spectra are noisier than those obtained with the 532 excitation (cf. Figures 7 and 8). On the other hand, our instrument for red Raman has a broader spectral range. We see the sulfhydryl group signaling at 2578 cm^{-1} (2500–2600 cm^{-1}, Tuma 2005) disappeared from the spectrum (Fig. 8, cf. b and d). This indicates formation of the S–Ag covalent bond during the SERS measurement. SERS GSH signals below 1000 cm^{-1} were enhanced (cf. b and d), the peptidic spectrum was ca 10,000× enhanced. SERS intensities induced with HCl (spectrum f) was even more enhanced (~20,000×) and also more resembled native Raman (cf. b, c and f), except of the lack of the sulfhydryl group band (2578 cm^{-1}). The higher enhancement can be explained by formation of a third plasmonic band of the pink silver during the induced SERS

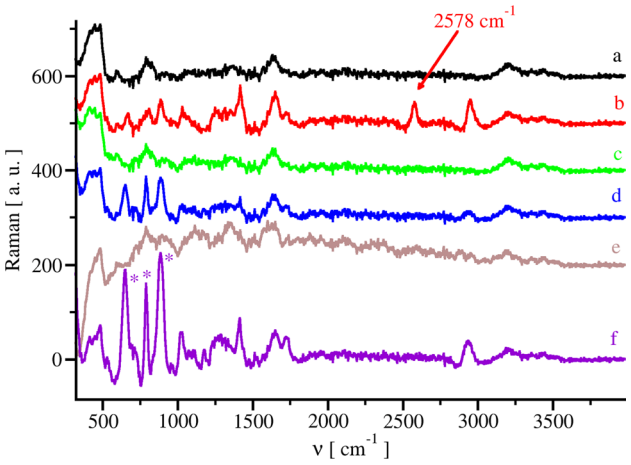

Fig. 8 Detection of GSH using pink silver and red laser 785 nm (300 mW, 300 ms integration time, 30 min accumulation, ~100 µM for SERS and 1 M for Raman of GSH). **a** water; **b** GSH+water; **c** pink sol; **d** GSH+pink sol; **e** pink sol+HCl; **f** GSH+pink sol+HCl. Asterisks are placed close to maxima with frequencies at 652 cm^{-1}, 789 cm^{-1}, and 886 cm^{-1}, respectively

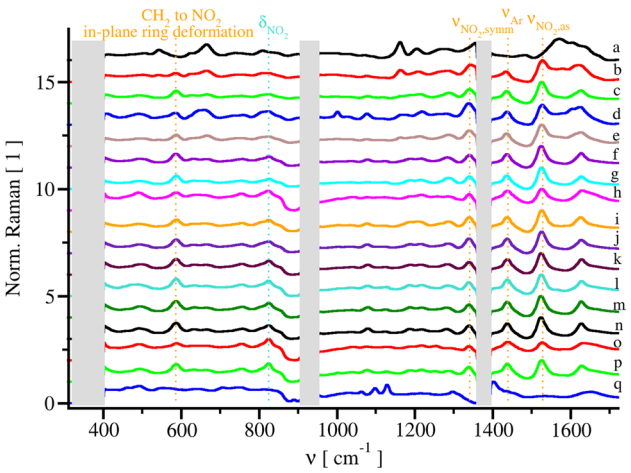

Fig. 9 SERS spectra of variously nitrated peptide observed with the pink silver and green laser (532 nm, 300 mW, 3.08 s illumination time, ~100 µM). ACN signals at 383, 924 and 1376 cm^{-1} are hidden by the gray bars. **a** YYACAYY; **b** YYACAYNit; **c** YYACANitY; **d** YNitACAYY; **e** NitYACAYY; **f** YYACANitNit; **g** YNitACAYNit; **h** NitYACAYNit; **i** YNitACANitY; **j** NitYACANitY; **k** NitNitACAYY; **l** YNitACANitNit; **m** NitYACANitNit; **n** NitNitACAYNit; **o** NitNitACANitY; **p** NitNitACANitNit; **q** Pink silver+ACN (blank)

conditions (see also Figure S5). The most intense bands at 652 cm^{-1}, 789 cm^{-1}, and 886 cm^{-1} (Fig. 8f) correspond to C–S stretching, $–COO^-$ bending, and C–C stretching, respectively (Huang et al. 2010).

The pink silver was examined for detection of the YYACAYY nitration with green laser (532 nm) under the native and induced SERS conditions. For the native

SERS (Fig. 9), very strong signal of asymmetric nitro band (1523–1527 cm^{-1}, $\nu_{NO2,as}$) was observed. It is also possible to see symmetric nitro band (1338–1343 cm^{-1}, $\nu_{NO2,symm}$), which is very close to suppressed signal of ACN at 1376 cm^{-1}. For those model peptides, there were identified other two markers for nitration i.e. bands at 585–590 cm^{-1}, and at 1434–1440 cm^{-1}. The group can be attributed to in-plane ring deformation involving β-CH_2 and NO_2 groups, whereas the second one comes from the substituted aromatic ring. On the other hand, the bending δ_{NO2} vibration is very weak under the native SERS conditions and tyrosine does not have the characteristic double band on pink silver in native peptides (Fig. 9a).

For induced SERS (Figure S7), a weak signal of asymmetric nitro vibration (1523–1527 cm^{-1}, $\nu_{NO2,as}$) was observed. Thus $\nu_{NO2,as}$ is strong under native SERS and weak under induced SERS. Perhaps this can be attributed to different ionic form of Nit. Under induced SERS in low pH the phenolic oxygen is protonated and UV–Vis spectrum of Nit is blue shifted (Beeckmans and Kanarek 1983; De Filippis et al. 2006; Yang et al. 2010). Native condition works with pH around 7, where Nit phenolate is partially deprotonated and UV–Vis spectrum is red shifted (Beeckmans and Kanarek 1983; De Filippis et al. 2006; Yang et al. 2010). The red shift can cause overlap between silver plasmonic band and nitrophenolate electronic excitations, leading to surface enhanced resonance Raman spectra (SERRS) (Smith and Dent 2019).

As we have previously shown with different types of silver colloids (brown-yellow silvers) under induced SERS condition (Niederhafner et al. 2021), another nitration marker can be observed in the δ_{NO2} region (828–880 cm^{-1}) overlapping with a tyrosine double band [around 825–870 cm^{-1} (Tuma 2005; Rygula et al. 2013), out-of-plane H-C bend (η_{HC}, 825 cm^{-1}) and ring breathing (β_{CCC}, 850 cm^{-1})]. After the nitration, relative magnitudes of the two bands become opposite due to overlap with δ_{NO2} signal and perturbation of the ring symmetry (Niederhafner et al. 2021). With the pink silver and YYACAYY peptides, instead of the characteristic doublet, a triplet was observed at 803, 829, and 852 cm^{-1} for the wild-type peptide model (Figure S7a). After the nitration, the region was dominated by δ_{NO2} bands at 823–827 cm^{-1} overlapping with the triplet. Thus the behavior of the δ_{NO2} vibration on the pink and brown-yellow silver is similar.

The detection of Nit was also tried with the red laser (785 nm, Fig. 10). Since the red wavelength is far from the absorption maxima of nitrotyrosine (Beeckmans and Kanarek 1983; De Filippis et al. 2006; Yang et al. 2010), non-resonance SERS occurs. Neither $\nu_{NO2,as}$ nor $\nu_{NO2,symm}$ could be observed, but the δ_{NO2} bands at 823–827 cm^{-1} became dominant (Fig. 10), in some cases stronger than the ACN vibration at 924 cm^{-1}. The signal at 803 cm^{-1} was

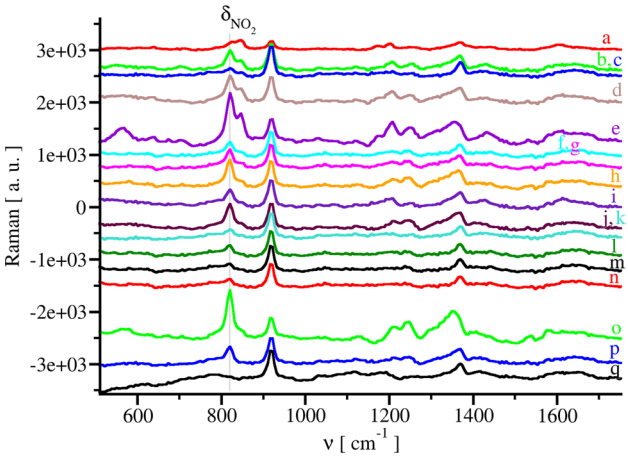

Fig. 10 SERS spectra of variously nitrated peptide, using induced SERS pink silver and red laser 785 nm, 300 mW, 300 ms integration time, 30 min accumulation, ~ 100 µM. **a** YYACAYY; **b** YYACAYNit; **c** YYACANitY; **d** YNitACAYY; **e** NitYACAYY; f) YYACANitNit; **g** YNitACAYNit; **h** NitYACAYNit; **i** YNitACANitY; **j** NitYACANitY; **k** NitNitACAYY; **l** YNitACANitNit; **m** NitYACANitNit; **n** NitNitACAYNit; **o** NitNitACANitY; **p** NitNitACANitNit; **q** Pink silver + ACN + 1 M HCl (blank)

negligible, and the spectral motif around the δ_{NO2} band resembles that one observed earlier with brown-yellow silver and green laser excitation (Niederhafner et al. 2021).

Using native SERS with green light excitation, $\nu_{NO2,as}$ band could be detected down to 114 nM (Figure S8), ca at 4 times lower concentration than for GSH (Fig. 7). The presence of the nitro group allowed to detect the peptides at lower concentration than without it. At induced SERS the δ_{NO2} band was detectable down to 1.04 µM (Figure S9). Thus the native SERS provided about one order of magnitude lower limit of detection than the induced one.

Calculation of SERS spectra

SERS spectra of YYACAYY peptide at various orientations to the silver surface were calculated at two levels, directly using the HF/LanL2MB/CPCM(water) method, and by the "CTT" transfer of tensors (vibrational parameters) calculated for small fragments at the B3PW91/LanL2DZ/CPCM(water) level (Figure S10). The calculated relative band intensities were not too realistic (cf. a–b and c–f), perhaps due to a resonance enhancement, the calculated frequencies were slightly shifted to higher wavenumbers if compared to experiment.

As a simplified model, we also used the Ac-Tyr-NHMe molecule in different charged forms bound to the silver surface. In the parent peptide, monomers 1 and 2 dominate the spectrum (cf Figure S11 and Fig. 11g). Monomer 2 was selected for simplified simulations of silver bound phenolate, nitrophenolate and two isomers of nitrophenol (Fig. 11). Calculated spectrum of a conformer of YYACAYY bound

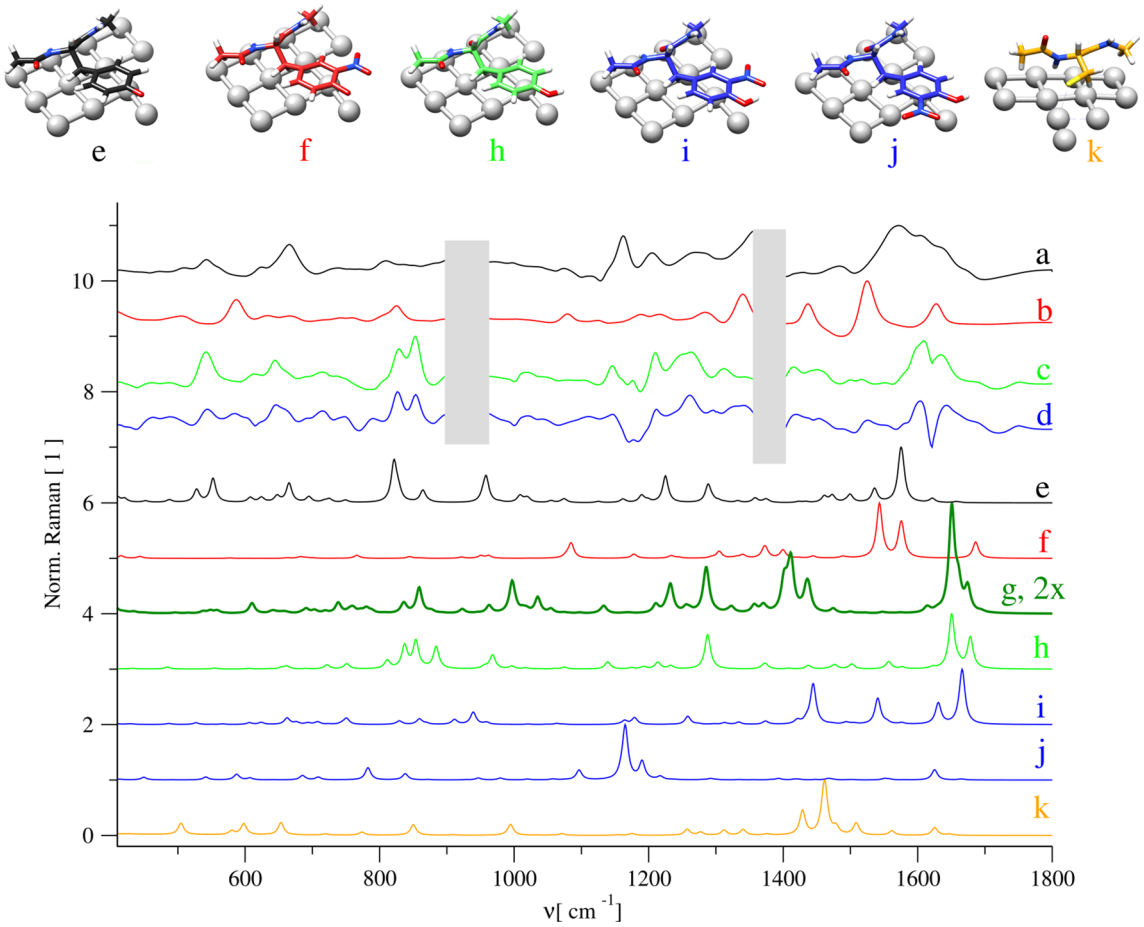

Fig. 11 Structures, experimental (**a**–**d**) and calculated (**e**–**k**) SERS spectra, **a** native SERS of YYACAYY; **b** native SERS of NitNitACAYY; **c** induced SERS of YYACAYY; **d** induced SERS of NitNitACAYY; **e** calculated SERS of Ac-Tyr(anion)-NHMe (monomer 2); **f** calculated SERS of Ac-Nit(anion)-NHMe (monomer 2); **g** calculated SERS of YYACAYY peptide one conformer in plane orientation; **h** calculated SERS of Ac-Tyr-NHMe (monomer 2); **i** calculated SERS of Ac-Nit-NHMe (monomer 2, close form); **j** calculated SERS of Ac-Nit-NHMe (monomer 2, open form); **k** calculated SERS of Ac-Cys(Ag@sol)-NHMe (monomer 4). In experimental spectra, the ACN band were suppressed. Original structures **h** and **k** were obtained from one representation of YYACAYY peptide bound on silver surface in plane mode. Other structures were derived from model Ac-Tyr-NHMe (h, monomer 2): **e** phenolate; **f** nitrophenolate; **i** close nitrophenol; and **j** open nitrophenol

to silver surface is shown in Fig. 11g. The characteristic tyrosine double band (825–875 cm^{-1}) is partially reproduced for the neutral species (Fig. 11c and h). We are aware that this approach is a simplification, but it can explain at least some observed phenomena. If we compare native SERS of the NitNitACAYY peptide with the calculated spectrum of Ac-Nit(anion)-NHMe (Fig. 11b and f), there is a good agreement with the experiment above 1079 cm^{-1}. This region is dominated by resonance enhanced nitrophenolate bands. The region below 1079 cm^{-1} contains also bands related to the binding of sulfur side chain and nitrogen backbone to the silver surface, not included in the model.

Another limitation of the model is the system geometry and silver cluster shape. As we have shown previously, an alteration of analyte-silver orientation can change the spectrum (Hamissa et al. 2022). In order to better understand this factor, we have increased the amount of selected silver atoms (Figure S12). Addition of four silver atoms led to more symmetric silver surface and enhancement of many vibrational modes of Ac-Tyr-NHMe (Figure S12, cf spectra a and b). Another addition of four silver atoms led to amplification of the aromatic and amide III bands (Figure S12c) and the benzene hydrogen stretching bands (Figure S12d). A shift of one silver atom from original crystal to more symmetrical silver surface suppressed this enhancement (cf. d and e). Addition of four atoms from the second silver layer to structure b (Figure S12) led to amplification of aromatic and amide III vibrations, similarly to c, and the amide I vibration was also enhanced (cf. c and f). Further extension by a third set of four silver atoms led to enhancement of the amide I band (Figure S12 g,h).

Conclusions

We were able to photochemically synthesize a new SERS substrate, the pink silver. It proved to be useful for sensitive detection of the peptide tyrosine nitration. We have investigated two SERS protocols, with native colloids and with induced aggregation by HCl. The native one provides four vibrational markers for nitrated tyrosine, the most intense of which is asymmetric NO_2 vibration (1523–1530 cm^{-1}), and the peptide nitration can be detected down to 114 nM concentration. For the induced mode, the NO_2 bending vibration (815–827 cm^{-1}) was the most suitable marker. The results are thus promising for usage of silver SERS in monitoring of biological processes associated with the oxidative stress.

Supplementary Information The online version contains supplementary material available at https://doi.org/10.1007/s00726-022-03178-w.

Acknowledgements This work was supported by the Czech Science Foundation (22-04669S), Research Project RVO 61388963, by European Regional Development Fund; OP RDE; Project: "Chemical biology for drugging undruggable targets (ChemBioDrug)" (No. CZ.02.1.01/0.0/0.0/16_019/0000729). Computational resources were supplied by the project "e-Infrastruktura CZ" (e-INFRA CZ LM2018140) supported by the Ministry of Education, Youth and Sports of the Czech Republic. MT and JŠ thank for support from ORLEN Unipetrol Foundation provided to Mensa Gymnázium. Also, we thank Dr. Jan Ježek, Ph. D. for the corrections of English language. The molecular structures were visualized using program UCSF Chimera (Pettersen et al. 2004).

Declarations

Conflict of interest The authors declare that they have no conflict of interest.

Informed consent This paper does not contain any studies with human participants or animals performed by any of the authors. For this type of study formal consent is not required.

References

Abello N, Kerstjens HA, Postma DS, Bischoff R (2009) Protein tyrosine nitration: selectivity, physicochemical and biological consequences, dinitration and proteomic methods for the identification of tyrosine-nitrated proteins. J Proteome Res 8(7):3222–3238

Abello N, Barroso B, Kerstjens HAM, Postma DS, Bischoff R (2010) Chemical labeling and enrichment of nitrotyrosine-containing peptides. Talanta 80:1503–1512

Alvarez-Puebla RA, Contreras-Caceres R, Pastoriza-Santos I, Perez-Juste J, Liz-Marzan LM (2009) Au@pNIPAM colloids as a molecular traps for surface-enhanced, spectroscopic, ultra-sensitive analysis. Angew Chem Int Ed 48(1):138–143

Aslan M, Dogan S (2011) Proteomic detection of nitroproteins as potential biomarkers for cardiovascular disease. J Proteomics 74(11):2274–2288

Beal MF, Ferrante RJ, Browne SE, Matthews RT, Kowall NW, Brown RH Jr (1997) Increased 3-nitrotyrosine in both sporadic and familial amyotropic lateral sclerosis. Ann Neurol 42(4):644–654

Beckman JS, Crow JP (1993) Pathological implications of nitric oxide, superoxide and peroxynitrite formation. Biochem Soc Trans 21(2):330–334

Beckman JS, Beckman TW, Chen J, Marshall PA, Freeman BA (1990) Apparent hydroxyl radical production by peroxynitrite: implications for endothelial injury from nitric oxide and superoxide. Proc Natl Acad Sci USA 87(4):1620–1624

Beeckmans S, Kanarek L (1983) The modification with tetranitromethane of an essential tyrosine in the active site of pig fumarase. Biochim Biophys Acta 743:370–378

Betz JF, Yu WW, Cheng Y, White IM, Rubloff GW (2014) Simple SERS substrates: powerful, portable, and full of potential. Phys Chem Chem Phys 16(6):2224–2239

Bouř P, Keiderling TA (2002) Partial optimization of molecular geometry in normal coordinates and use as a tool for simulation of vibrational spectra. J Chem Phys 117(9):4126–4132

Bouř P, Sopková J, Bednarová L, Maloň P, Keiderling TA (1997) Transfer of molecular property tensors in cartesian coordinates: a new algorithm for simulation of vibrational spectra. J Comput Chem 18(5):646–659

Burai R, Ait-Bouziad N, Chiki A, Lashuel HA (2015) Elucidating the role of site-specific nitration of α-synuclein in the pathogenesis of Parkinson's disease via protein semisynthesis and mutagenesis. J Am Chem Soc 137(15):5041–5052

Campolo N, Issoglio FM, Estrin DA, Bartesaghi S, Radi R (2020) 3-Nitrotyrosine and related derivatives in proteins: precursors, radical intermediates and impact in function. Essays Biochem 64(1):111–133

Case DA et al (2012) AMBER 12. University of California, San Francisco

Castro L, Demicheli V, Tortora V, Radi R (2011) Mitochondrial protein tyrosine nitration. Free Radic Res 45(1):37–52

Chang C-Y, Chen Y-M, Huang Y-B, Lai C-H, Jeng U-S, Lai Y-H (2019) Nanostructured silver dendrites for photon-induced cysteine dimerization. Sci Rep 9:20174

Das M, Gangopadhyay D, Šebestík J, Habartová L, Michal P, Kapitán J, Bouř P (2021) Chiral detection by induced surface-enhanced Raman optical activity. Chem Comm 57:6388–6391. https://doi.org/10.1039/d1cc01504d

De Filippis V, Frasson R, Fontana A (2006) 3-Nitrotyrosine as a spectroscopic probe for investigating protein-protein interactions. Protein Sci 15:976–986

Duda JE, Giasson BI, Chen Q, Gur TL, Hurtig HI, Stern MB, Gollomp SM, Ischiropoulos H, Lee VM, Trojanowski JQ (2000) Widespread nitration of pathological inclusions in neurodegenerative synucleinopathies. Am J Pathol 157(5):1439–1445

Félix-Domínguez F, Carrillo-Torres RC, Lucero-Acuña A, Sánchez-Zeferino R, Álvarez-Ramos ME (2019) Seedless synthesis of silver nanoparticles using sunlight and study of the effect of different ratios of precursors. Mater Res Express 6:045067

Ferrer-Sueta G, Campolo N, Trujillo M, Bartesaghi S, Carballal S, Romero N, Alvarez B, Radi R (2018) Biochemistry of peroxynitrite and protein tyrosine nitration. Chem Rev 118(3):1338–1408

Fields GB, Noble RL (1990) Solid phase peptide synthesis utilizing 9-fluorenylmethoxycarbonyl amino acids. Int J Pept Prot Res 35(3):161–214

Forman HJ, Zhang H (2021) Targeting oxidative stress in disease: promise and limitations of antioxidant therapy. Nature Rev Drug Discovery 20:689–709

Frisch MJ, Trucks GW, Schlegel HB, Scuseria GE, Robb MA, Cheeseman JR, Scalmani G, Barone V, Petersson GA, Nakatsuji H, Li X, Caricato M, Marenich AV, Bloino J, Janesko BG, Gomperts R, Mennucci B, Hratchian HP, Ortiz JV, Izmaylov AF, Sonnenberg JL, Williams-Young D, Ding F, Lipparini F, Egidi F, Goings J, Peng B, Petrone A, Henderson T, Ranasinghe D, Zakrzewski VG,

Gao J, Rega N, Zheng G, Liang W, Hada M, Ehara M, Toyota K, Fukuda R, Hasegawa J, Ishida M, Nakajima T, Honda Y, Kitao O, Nakai H, Vreven T, Throssell K, Montgomery JA Jr, Peralta JE, Ogliaro F, Bearpark MJ, Heyd JJ, Brothers EN, Kudin KN, Staroverov VN, Keith TA, Kobayashi R, Normand J, Raghavachari K, Rendell AP, Burant JC, Iyengar SS, Tomasi J, Cossi M, Millam JM, Klene M, Adamo C, Cammi R, Ochterski JW, Martin RL, Morokuma K, Farkas O, Foresman JB, Fox DJ (2016) Gaussian 16 revision C.01. Gaussian Inc, Wallingford

Furth AJ, Hope DB (1970) Studies on the chemical modification of the tyrosine residue in bovine neurophysin-II. Biochem J 116:545–553

Giasson BI, Duda JE, Murray IVJ, Chen Q, Souza JM, Hurtig HI, Ischiropoulos H, Trojanowski JQ, Lee VM-Y (2000) Oxidative damage linked to neurodegeneration by selective α-synuclein nitration in synucleinopathy lesions. Science 290(5493):985–989

Graham D, Thompson DG, Smith WE, Faulds K (2008) Control of enhanced Raman scattering using a DNA-based assembly process of dye-coded nanoparticles. Nat Nanotechnol 3(9):548–551

Guerrini L, Graham D (2012) Molecularly-mediated assemblies of plasmonic nanoparticles for surface-enhanced Raman spectroscopy applications. Chem Soc Rev 41:7085–7107

Gupta M, Paliwal VK, Babu GN (2021) Serum fractalkine and 3-nitrotyrosine levels correlate with disease severity in Parkinson's disease: a pilot study. Metab Brain Dis. https://doi.org/10.1007/s11011-021-00801-9

Hamissa MF, Niederhafner P, Šestáková H, Šafařík M, Hadravová R, Šebestík J (2022) Neutral and charged forms of inubosin B in aqueous solutions at different pH and on the surface of Ag nanoparticles. J Mol Struct 1250(2):131828

Heinz H, Farmer BL, Naik RR (2008) Accurate simulation of surfaces and interfaces of face-centered cubic metals using 12–6 and 9–6 Lennard-Jones potentials. J Phys Chem C 112:17281–17290

Heinz H, Farmer BL, Pandey RB, Slocik JM, Patnaik SS, Pachter R, Naik RR (2009) Nature of molecular interactions of peptides with gold, palladium, and Pd-Au bimetal surfaces in aqueous solution. J Am Chem Soc 131:9704–9714

Huang GG, Han XX, Hossain MK, Kitahama Y, Ozaki Y (2010) A study of glutathione molecules adsorbed on silver surfaces under different chemical environments by surface-enhanced Raman scattering in combination with the heat-induced sensing method. Appl Spectrosc 64(10):1100–1108

Huang CL, Chen SH, Wu CY, Sie YS, Kao PC (2019) Influence of the silver nanocrystal shape on the luminous efficiency of blue-emitting polymer light-emitting diodes. Langmuir 35(47):15114–15120

Jalili R, Dastborhan M, Chenaghlou S, Khataee A (2020) Incorporating of gold nanoclusters into metal-organic frameworks for highly sensitive detection of 3-nitrotyrosine as an oxidative stress biomarker. J Photochem Photobiol A 391:112370

Ježek J, Hlaváček J, Šebestík J (2017) Applications for treatment of neurodegenerative diseases. Prog Drug Res 72:99–134

Jing H, Zhang Q, Large N, Yu C, Blom DA, Nordlander P, Wang H (2014) Tunable plasmonic nanoparticles with catalytically active high-index facets. Nano Lett 14(6):3674–3682

Klamt A, Schüürmann G (1993) COSMO: a new approach to dielectric screening in solvents with explicit expressions for the screening energy and its gradient. J Chem Soc Perkin Trans A 2(5):799–805

Kleinman SL, Frontiera RR, Henry AI, Dieringer JA, Van Duyne RP (2013) Creating, characterizing and controlling chemistry with SERS hot spots. Phys Chem Chem Phys 15(1):21–36

Kummer MP, Hermes M, Delekarte A, Hammerschmidt T, Kumar S, Terwel D, Walter J, Pape H-C, König S, Roeber S, Jessen F, Klockgether T, Korte M, Heneka MT (2011) Nitration of tyrosine 10 critically enhances amyloid β aggregation and plaque formation. Neuron 71(5):833–844

Kurouski D, Van Duyne RP (2015) In situ detection and identification of hair dyes using surface-enhanced Raman spectroscopy (SERS). Anal Chem 87(5):2901–2906

Kurouski D, Lee H, Roschangar F, Senanayake Ch (2017) Surface-enhanced Raman spectroscopy: from concept to practical application. Spectroscopy 32(11):36–44

Larsen MR, Trelle MB, Thingholm TE, Jensen ON (2006) Analysis of posttranslational modifications of proteins by tandem mass spectrometry. Biotechniques 40(6):790–798

Lee J, Choe IR, Kim N-K, Kim W-J, Jang H-S, Lee Y-S, Nam KT (2016) Water-floating giant nanosheets from helical peptide pentamers. ACS Nano 10(9):8263–8270

Lee J, Ju M, Cho OH, Kim Y, Nam KT (2019) Tyrosine-rich peptides as a platform for assembly and material synthesis. Adv Sci 6:1801255

Leopold N, Lendl B (2003) A new method for fast preparation of highly surface-enhanced Raman scattering (SERS) active silver colloids at room temperature by reduction of silver nitrate with hydroxylamine hydrochloride. J Phys Chem B 107(24):5723–5727

Li Y-T, Li D-W, Cao Y, Long Y-T (2015) Label-free in-situ monitoring of protein tyrosine nitration in blood by surface-enhanced Raman spectroscopy. Biosens Bioelectron 69:1–7

Liu Y, Zhou P, Da H, Jia H, Bai F, Hu G, Zhang B, Fang J (2019) An Azo coupling strategy for protein 3-nitrotyrosine derivatization. Chem Eur J 25:11228–11232

Madkour LH (2019) Function of reactive oxygen species (ROS) inside the living organisms and sources of oxidants. J Glob Pharma Technol 2(2):1–23

Martins GV, Marques AC, Fortunato E, Sales MGF (2018) Wax-printed paper-based device for direct electrochemical detection of 3-nitrotyrosine. Electrochim Acta 284:60–68

Martins GV, Marques AC, Fortunato E, Sales MGF (2020) Paper-based (bio)sensor for label-free detection of 3-nitrotyrosine in human urine samples using molecular imprinted polymer. Sens Bio-Sens Res 28:100333

Martinsson E, Shahjamali MM, Large N, Zaraee N, Schatz GC, Aili D, Mirkin CA (2015) Influence of surfactant bilayers on the refractive index sensitivity and catalytic properties of anisotropic gold nanoparticles. Small 12(3):330–342

Meade RM, Fairlie DP, Mason JM (2019) Alpha-synuclein structure and Parkinson's disease—lessons and emerging principles. Mol Neurodegener 14:29

Mulfinger L, Solomon SD, Bahadory M, Jeyarajasingam AV, Rutkowsky SA, Boritz C (2007) Synthesis and Study of Silver Nanoparticles. J Chem Educ 84(2):322–325. https://doi.org/10.1021/ed084p322

Mulvihill MJ, Ling XY, Henzie J, Yang P (2010) Anisotropic etching of silver nanoparticles for plasmonic structures capable of single-particle SERS. J Am Chem Soc 132(1):268–274

Niederhafner P, Šafařík M, Brichtová E, Šebestík J (2016) Rapid acidolysis of benzyl group as a suitable approach for synthesis of peptides naturally produced by oxidative stress and containing 3-nitrotyrosine. Amino Acids 48(4):1087–1098

Niederhafner P, Šafařík M, Neburková J, Keiderling TA, Bouř P, Šebestík J (2021) Monitoring peptide tyrosine nitration by spectroscopic methods. Amino Acids 53:517–532

Oueslati A, Fournier M, Lashuel HA (2010) Role of post-translational modifications in modulating of structure, function and toxicity of alpha-synuclein. Implications for Parkinson's disease pathogenesis and therapies. Progress Brain Res 183(C):115–145

Özmetin C, Çopur M, Kocakerim MM, Yapici S (2001) Crystallization of silver nitrate from saturated silver nitrate solution in nitric acid. Indian J Chem Technol 8:112–119

Perdew JP, Burke K, Wang Y (1996) Generalized gradient approximation for the exchange-correlation hole of a many-electron system. Phys Rev B 54(23):16533–16539

Pettersen EF, Goddard TD, Huang CC, Couch GS, Greenblatt DM, Meng EC, Ferrin TE (2004) UCSF chimera—a visualization system for exploratory research and analysis. J Comput Chem 25(13):1605–1612

Pezzotti G, Boschetto F, Ohgitani E, Fujita Y, Shin-Ya M, Adachi T, Yamamoto T, Kanamura N, Marin E, Zhu W, Nishimura I, Mazda O (2021) Mechanisms of instantaneous inactivation of SARS-CoV-2 by silicon nitride bioceramic. Mater Today Bio 12:100144

Radi R (2004) Nitric oxide, oxidants, and protein tyrosine nitration. Proc Natl Acad Sci USA 101(12):4003–4008

Radi R (2013) Protein tyrosine nitration: biochemical mechanisms and structural basis of functional effects. Acc Chem Res 46(2):550–559

Reynolds MR, Berry RW, Binder LI (2005) Site specific nitration and oxidative dityrosine bridging of the tau protein by peroxynitrite: Implications for Alzheimer's disease. Biochemistry 44(5):1690–1700

Ruud K, Thorvaldsen AJ (2009) Theoretical approaches to the calculation of Raman optical activity spectra. Chirality 21:E54–E67

Rycenga M, Langille MR, Personick ML, Ozel T, Mirkin CA (2012) Chemically isolating hot spots on concave nanocubes. Nano Lett 12(12):6218–6222

Rygula A, Majzner K, Marzec KM, Kaczor A, Pilarczyk M, Baranska M (2013) Raman spectroscopy of proteins: a review. J Raman Spectrosc 44(8):1061–1076

Sangsuwan R, Obermeyer AC, Tachachartvanich P, Palaniappan KK, Francis MB (2016) Direct detection of nitrotyrosine-containing proteins using an aniline-based oxidative coupling strategy. Chem Commun 52:10036–10039

Seballos L, Richards N, Stevens DJ, Patel M, Kapitzky L, Lokey S, Millhauser G, Zhang JZ (2007) Competitive binding effects on surface-enhanced Raman scattering of peptide molecules. Chem Phys Lett 447(4–6):335–339

Šebestík J, Bouř P (2011) Raman optical activity of methyloxirane gas and liquid. J Phys Chem Lett 2(5):498–502

Šebestík J, Šafařík M, Bouř P (2012) Ferric complexes of 3-hydroxy-4-pyridinones characterized by density functional theory and Raman and UV-vis spectroscopies. Inorg Chem 51(8):4473–4481

Seeley KW, Fertig AR, Dufresne CP, Pinho JPC, Stevens SM Jr (2014) Evaluation of a method for nitrotyrosine site identification and relative quantitation using a stable isotope-labeled nitrated spike-in standard and high resolution Fourier transform MS and MS/MS analysis. Int J Mol Sci 15:6265–6285

Sevcsik E, Trexler AJ, Dunn JM, Rhoades E (2011) Allostery in a disordered protein: oxidative modifications to α-synuclein act distally to regulate membrane binding. J Am Chem Soc 133(18):7152–7158

Shao Z, Zhu W, Wang H, Yang Q, Yang S, Liu X, Wang G (2013) Controllable synthesis of concave nanocubes, right bipyramids, and 5-fold twinned nanorods of palladium and their enhanced electrocatalytic performance. J Phys Chem C 117(27):14289–14294

Sharma B, Frontiera RR, Henry AI, Ringe E, Van Duyne RP (2012) SERS: material, applications and the future. Mater Today 15(1–2):16–25

Sharov VS, Dremina ES, Galeva NA, Stobaugh JF, Schoneich C (2010) Reduction of protein/peptide 3-nitrotyrosine to 3-aminotyrosine by sodium dithionite: optimization of reaction conditions for proteomic analysis of 3-nitrotyrosine *via* fluorogenic and affinity tagging. Free Radical Biol Med 49:S88–S89

Sies H (2020) Oxidative stress: concept and some practical aspects. Antioxidants 9(9):852

Smith E, Dent G (2019) Surface enhanced Raman scattering and surface enhanced resonance Raman scattering. In: Smith E, Dent G (eds) Modern Raman spectroscopy. Wiley, pp 119–149

Soderling A-S, Hultman L, Delbro D, Hojrup P, Caidahl K (2007) Reduction of the nitro group during sample preparation may cause underestimation of the nitration level in 3-nitrotyrosine immunoblotting. J Chromatogr B 851:277–286

Spears RJ, McMahon C, Chudasama V (2021) Cysteine protecting groups: applications in peptide and protein science. Chem Soc Rev 50:11098–11155

Sue Legge F, Nyberg GL, Barrie Peel J (2001) DFT Calculations for Cu-, Ag-, and Au-containing molecules. J Phys Chem A 105(33):7905–7916

Taylor RW, Lee TC, Scherman OA, Esteban R, Aizpurua J, Huang FM, Baumberg JJ, Mahajan S (2011) Precise subnanometer plasmonic junctions for SERS within gold nanoparticle assemblies using cucurbit [n]uril "glue." ACS Nano 5(5):3878–3887

Tomasi J, Mennucci B, Cammi R (2005) Quantum mechanical continuum solvation models. Chem Rev 105:2999–3093

Tsikas D, Duncan MW (2014) Mass spectrometry and 3-nitrotyrosine: strategies, controversies, and our current perspective. Mass Spectrom Rev 33(4):237–276

Tuma R (2005) Raman spectroscopy of proteins: from peptides to large assemblies. J Raman Spectrosc 36(4):307–319

van Haandel L, Killmer J, Li X, Schoneich C, Stobaugh JF (2008) Phenylisothiocyanate as a multiple chemical dimension reagent for the relative quantitation of protein nitrotyrosine. Chromatographia 68:507–516

Vana L, Kanaan NM, Hakala K, Weintraub ST, Binder LI (2011) Peroxynitrite-induced nitrative and oxidative modifications alter tau filament formation. Biochemistry 50(7):1203–1212

Xue C, Métraux GS, Millstone JE, Mirkin CA (2008) Mechanistic study of photomediated triangular silver nanoprism growth. J Am Chem Soc 130:8337–8344

Yamamoto S, Bouř P (2013) Transition polarizability model of induced resonance Raman optical activity. J Comput Chem 34(25):2152–2158

Yang H, Zhang Y, Pöschl U (2010) Quantification of nitrotyrosine in nitrated proteins. Anal Bioanal Chem 397:879–886

Yang L-C, Lai Y-S, Tsai C-M, Kong Y-T, Lee C-I, Huang C-L (2012) One-pot synthesis of monodispersed silver nanodecahedra with optimal SERS activities using seedless photo-assisted citrate reduction method. J Phys Chem C 116:24292–24300

Yttenberg AJ, Jensen ON (2010) Modification-specific proteomics in plant biology. J Proteomics 73(11):2249–2266

Zhai H, Wang S, Zhou J, Pan J, Tong Y, Mei Q, Zhou Q (2019) A simple and sensitive electrochemical sensor for 3-nitrotyrosine based on electrochemically anodic pretreated glassy carbon electrode in anionic surfactant medium. J Electrochem Soc 166:B1426–B1433

Zhang Q, Large N, Nordlander P, Wang H (2014a) Porous Au nanoparticles with tunable plasmon resonances and intense field enhancements for single-particle SERS. J Phys Chem Lett 5(2):370–374

Zhang Q, Large N, Wang H (2014b) Gold nanoparticles with tipped surface structures as substrates for single-particle surface-enhanced Raman spectroscopy: concave nanocubes, nanotrisoctahedra, and nanostars. ACS Appl Mater Interf 6(19):17255–17267

Zhao Y, Zhang Y, Sun H, Maroto R, Brasier AR (2017) Selective affinity enrichment of nitrotyrosine-containing peptides for quantitative analysis in complex samples. J Proteome Res 16(8):2983–2992